

1 Present kinematics of the Tjörnes Fracture Zone, North 2 Iceland, from campaign and continuous GPS measurements

3
Sabrina Metzger¹, Sigurjón Jónsson², Gillis Danielsen², Sigrún Hreinsdóttir³, François Jouanne⁴,
Domenico Giardini¹, Thierry Villemin⁴*

¹*Institute of Geophysics, ETH Zürich, Sonneggstrasse 5, 8092 Zürich, Switzerland*

²*King Abdullah University of Science and Technology (KAUST), Thuwal, Saudi Arabia*

³*Nordic Volcanological Center, Institute of Earth Sciences, University of Iceland, Iceland*

⁴*Université de Savoie, Bourget-du-Lac, France*

4 5 **SUMMARY**

6 The Tjörnes Fracture Zone (TFZ), North Iceland, is a 120 km transform offset of the
7 Mid-Atlantic-Ridge that accommodates 18 mm yr^{-1} plate motion on two parallel trans-
8 form structures and connects the offshore Kolbeinsey Ridge in the North to the on-shore
9 Northern Volcanic Zone (NVZ) in the South. This transform zone is offshore except for
10 a part of the right-lateral strike-slip Húsavík-Flatey fault (HFF) system that lies close to
11 the coastal town of Húsavík, inducing a significant seismic risk to its inhabitants. In our
12 previous work we constrained the locking depth and slip-rate of the HFF using 4 years
13 of continuous GPS measurements and found that the accumulated slip-deficit on the fault
14 is equivalent to a $M_w 6.8 \pm 0.1$ earthquake, assuming a complete stress release in the last
15 major earthquakes in 1872 and a steady accumulation since then (Metzger et al. 2011).

16 In this paper we improve our previous analysis by adding 44 campaign GPS (EGPS) data
17 points, which have have been regularly observed since 1997. We extract the steady-state
18 interseismic velocities within the TFZ by correcting the GPS data for volcanic inflation

19 of Theistareykir – the westernmost volcano of the NVZ – using a model with a magma
20 volume increase of $25 \times 10^6 \text{ m}^3$, constrained by InSAR time-series analysis results.

21 The improved velocity field based on 58 GPS stations confirms the robustness of our
22 previous model and allows to better constrain the free model parameters. For the HFF
23 we find a slightly shallower locking depth of $\sim 6.2 \text{ km}$ and a slightly higher slip-rate of
24 $\sim 6.8 \text{ mm yr}^{-1}$ that again result in the same seismic potential equivalent to a $M_w 6.8$ earth-
25 quake. The much larger number of GPS velocities improves the statistically estimated
26 model parameter uncertainties by a factor of two, when compared to our previous study,
27 a result that we validate using Bayesian estimation.

28 **Key words:** Time series analysis, Satellite geodesy, Radar interferometry, Oceanic trans-
29 form and fracture zone processes, numerical approximations and analysis, kinematics of
30 crustal and mantle deformation.

31 1 INTRODUCTION

32 The Tjörnes Fracture Zone (TFZ) in North Iceland, is one of two transform zones in Iceland that
33 can produce magnitude ~ 7 strike-slip earthquakes with a recurrence interval of decades to centuries
34 (Einarsson 1991). Due to its mostly offshore location and its complex geometry, consisting of at least
35 two parallel transform structures, the detailed tectonics and kinematics of this plate boundary zone are
36 still not well understood. One of the main lineaments in the fracture zone, the Húsavík-Flatey fault
37 (HFF), has ruptured in major earthquakes in 1755 and 1872, which indicates that the interseismic pe-
38 riod of the earthquake cycle might end soon. It is therefore important to estimate the seismic potential
39 of this strike-slip fault and its implications for the inhabitants of Húsavík, a town located right on top
40 of the fault. One way to assess the seismic potential of a locked fault is to estimate the dimensions of
41 the locked fault plane (length and locking depth) and the accumulated slip deficit since the last major
42 earthquake, derived from interseismic deformation rates (Wesnousky 1986).

43 Several studies have provided information about the slip rate and the locking depth of the HFF.
44 An estimation of max. 60 km accumulated slip during the last 7-9 Myr from Sæmundsson (1974)
45 and Gudmundsson et al. (1993) results in an average slip rate of a max. $7\text{-}8 \text{ mm yr}^{-1}$. Rögnvaldsson
46 et al. (1998) analysed relative locations of 1400 earthquakes in 60 swarms within the TFZ 1994-1997

* smetzger@erdw.ethz.ch

47 with a vertical uncertainty <2 km and found that less than 10% of all events occur deeper than 10 km,
48 deducing a base of the brittle crust at 10 km. Velocities from the first three continuous GPS stations
49 in North Iceland that were installed in 2001/2002 suggest that the HFF accommodates 40% of the
50 total plate motion (Geirsson et al. 2006). Using a plate spreading velocity of 18 mm yr^{-1} (MORVEL,
51 DeMets et al. 2010) this corresponds to a slip rate of 7 mm yr^{-1} . Other slip rates derived from campaign
52 GPS data are in the range of $\sim 5 \text{ mm yr}^{-1}$ (Árnadóttir et al. 2009) to 8 mm yr^{-1} (Jouanne et al. 2006). In
53 addition, Árnadóttir et al. (2009) used modeling to constrain the locking depth of the HFF at shallow
54 5 km, but the data used were sparse near the HFF and thus the locking depth was poorly constrained.

55 In our previous study we presented data from 14 continuous GPS (CGPS) stations in North Ice-
56 land, most of which we installed in 2006 to monitor the surface deformation within the TFZ (Metzger
57 et al. 2011). We modeled the kinematics of the plate boundary in North Iceland with an interseismic
58 back-slip model based on 9 dislocations in an elastic half-space plus a Mogi source representing infla-
59 tion of the Theistareykir volcano (Fig. 1). Our aim was to estimate both the locking depth and the slip
60 rate of the HFF. We found a slip rate of $6.6 \pm 0.6 \text{ mm yr}^{-1}$ and a surprisingly shallow locking depth of
61 $6.3^{+1.7}_{-1.2}$ km. Furthermore the modeling revealed that the HFF accommodates only $34 \pm 3\%$ of the total
62 plate motion, while the majority of the transform motion must be taken up by the offshore Grímsey
63 Oblique Rift (GOR), the other main lineament of the TFZ. Assuming complete stress unloading in the
64 last major earthquakes in 1872 and steady stress accumulation since then, the seismic potential of a
65 complete rupture of the Húsavík-Flatey fault corresponds to a $M_w 6.8 \pm 0.1$ event (Metzger et al. 2011).

66 In this paper we improve the kinematic model of the Tjörnes Fracture Zone by adding 44 cam-
67 paign GPS (EGPS) observations to the 14 CGPS data to further constrain the model parameters of the
68 TFZ. In addition, we analyze the time evolution of the transient volcanic uplift at Theistareykir using
69 InSAR time-series analysis and remove this signal from the GPS data to obtain corrected interseis-
70 mic deformation rates. Due to the enhanced network density near the onshore part of HFF and across
71 the rift zone along the Krafla system we are able to better constrain all model parameters. After an
72 overview section of the tectonic setting in North Iceland we present a review of historical earthquakes
73 in the region. We then document the acquisition and processing of the campaign GPS data, explain
74 how we resolve the transient deformation signal using InSAR time-series analysis, and how we esti-
75 mate the steady interseismic velocities from both the EGPS and CGPS time-series. The last part of this
76 paper explains how we model the kinematics of the TFZ and derive best fit model parameters and their
77 uncertainties using two different approaches of uncertainty estimation. Finally the obtained results are
78 discussed and compared with earlier published kinematic parameters.

2 TECTONIC SETTING OF NORTH ICELAND

Iceland is located on the mid-Atlantic Ridge where the Eurasian and North American plate are separating at a rate of 18 mm yr^{-1} in a $\text{N}104.5^\circ\text{E}$ direction, according to the MORVEL plate-motion model (DeMets et al. 2010). The plate boundary zone in Iceland is a few tens of kilometer wide, crossing the island from the southwest to the northeast, and is mostly defined by volcanic zones (i.e. the Western, Eastern and Northern Volcanic Zones) that accommodate the spreading motion within several parallel and overlapping volcanic systems (Fig. 1). However the onshore part of the plate boundary is offset $\sim 100 \text{ km}$ towards east, resulting in two transform zones at the Southern and the Northern shore of the island. The Southern transform zone is called the South Iceland Seismic Zone and connects Reykjanes peninsula, a continuation of the Reykjanes Ridge, to the Eastern Volcanic Zone. It is completely onshore and consists of a series of parallel N-S trending strike-slip faults, sometimes referred to as *bookshelf faulting* (Einarsson 1991). The Northern transform zone is usually called the Tjörnes Fracture Zone (TFZ) and is of a completely different geometry. It consists of the 100 km-long Húsavík-Flatey fault (HFF) and a second lineament located Northeast of the HFF, the Grímsey Oblique Rift (GOR), that both connect the Northern Volcanic Zone (NVZ) to the Kolbeinsey Ridge (KR).

The plate boundary structures in the TFZ are primarily marked by fault surface traces and micro-seismicity. The HFF is a mostly off-shore strike-slip fault with a minor opening component. The WNW-oriented 90 km long main fault strand extends from the Theistareykir fissure swarm to the Eyjafjarðaráll Rift. This rift links the HFF and the Kolbeinsey Ridge, which is the northward continuation of the mid-Atlantic Ridge (Figure 1). The HFF has been active for as long as 7-9 Myr with an estimated cumulative displacement of max. 60 km and is older than the GOR (Sæmundsson 1974; Gudmundsson et al. 1993; Homberg et al. 2010). Fault surface traces between the coastal town Húsavík and the Theistareykir fissure swarm show several parallel branches and a slight bend at Húsavík leading to a NW-strike of the onshore part of the fault system. This change in strike results in an increasing opening component of the fault system, which is expressed in pull-apart structures (*sag ponds*) southeast of Húsavík. The southeastern part of the fault lacks micro-seismicity, particularly since the Krafla rifting-episode 1975-1984 (Tryggvason 1980; Björnsson 1985; Tryggvason 1984). One possible explanation for the low microseismicity is that the rifting episode released accumulated stress on the southeastern part of the HFF (Maccaferri et al. 2012).

The second main lineament in the TFZ is the Grímsey Oblique Rift. It is similar to the Reykjanes Peninsula in southwest Iceland, consisting of a set of parallel, N-S oriented faults exhibiting both normal and strike-slip faulting and it is volcanically active (Rögnvaldsson et al. 1998). In our previous

112 work we estimated that $66\pm 3\%$ of the total TFZ transform motion is accommodated by the GOR
 113 (Metzger et al. 2011) where as the rest is taken up by the HFF.

114 The Northern Volcanic Zone is a 40 km wide rift zone that extends from Vatnajökull glacier in
 115 Southeast Iceland to the north coast and the TFZ, consisting of five volcanic systems (from NNW to
 116 SSE): Theistareykir, Krafla, Fremrinámar, Askja and Kverkfjöll (Fig 1). It became active 7-9 Ma years
 117 ago after an eastward jump of the plate boundary (Sæmundsson 1974). The most recent rifting episode
 118 within the Northern Volcanic Zone took place in the Krafla volcanic system in 1975-1984 (Tryggvason
 119 1980; Björnsson 1985; Tryggvason 1984) with over 20 intrusive events and crustal widening amount-
 120 ing to an average of 5 m across the Krafla fissure swarm, corresponding to 275 years of plate spreading
 121 (Tryggvason 1994). After nine years the rifting episode stopped, but the extensional pulse continued
 122 to propagate away from the rift axis and over time slowly decayed in amplitude (Foulger et al. 1992;
 123 Heki et al. 1993; Hofton & Foulger 1996). Fifteen years later the influence of the rifting episode had
 124 diminished (Völksen 2000; Jouanne et al. in prep.). Other recent rifting episodes in the NVZ occurred
 125 in the Krafla volcanic system 1724-1729 and Askja volcanic system 1874-1875 (Sigurdsson & Sparks
 126 1978). Two minor rifting events took place in 1618 and 1885 in Theistareykir, the westernmost vol-
 127 canic system in the NVZ (Magnúsdóttir & Brandsdóttir 2011). Theistareykir has not erupted since
 128 2500 BP (Karl Grönvold, pers. comm. 2011) but between 2007 and 2009 it had a period of inflation
 129 with a maximum uplift rate of $\sim 3 \text{ cm yr}^{-1}$ in late 2008 (see section 5.1).

130 3 HISTORICAL EARTHQUAKES IN THE TJÖRNES FRACTURE ZONE

131 Knowledge of large historical earthquakes provides vital information on the average length of the
 132 earthquake cycle. The first instrumentally derived magnitude and location estimations of Icelandic
 133 earthquakes were available in the beginning of the last century. For older events we have to rely
 134 on historical accounts, which are far from being complete, and treat the available information with
 135 caution. Information on historical earthquakes in North Iceland dates back to 1260, when a large
 136 earthquake took place close to Flatey island (Fig. 1, Thoroddsen 1880, 1925), but accounts from the
 137 following 3-4 centuries are limited (Thorgeirsson 2012). Below we list the largest known earthquakes
 138 in the TFZ during the past 300 years with magnitude estimates as given in (Stefánsson et al. 2008).

139 In 1755 a M7 earthquake took place in Skjálíandi Bay, which was felt widely on Tjörnes Penin-
 140 sula as well as on the two peninsulas west of Skjálíandi Bay and caused damage to many buildings,
 141 open cracks and rock fall along the fjords (Thoroddsen 1925). Another earthquake happened near the
 142 northwestern end of the HFF in 1838 (M6.5). The next two large earthquakes on the HFF occurred 6
 143 hours apart in 1872 and the size of each has been estimated M6.5. The former event took place near
 144 Húsavík, causing fissures with up to 1 m of opening (Thoroddsen 1925, p.400), but the latter occurred

145 close to Flatey island. Other major events were the M6.2 earthquake close to the town of Dalvík in
146 1934 and a M7 earthquake in 1963 that was located ~ 60 km northwest of Dalvík. Due to these two
147 large events and some micro-seismicity Rögnvaldsson et al. (1998) and Stefánsson et al. (2008) have
148 suggested a third “weak” Dalvík zone southwest of the HFF with several N-S trending faults, similar
149 to the Grímsey Oblique Rift.

150 Known large earthquakes along the Grímsey Oblique Rift are a M6.3 earthquake in 1885 induced
151 by the Theistareykir rifting event at that time, a M7 earthquake in 1910 midway between the island
152 Grímsey and Öxarfjörður and a M6.2 earthquake in 1976 at the northern end of the Krafla fissure
153 swarm. The last one mentioned was part of the initial phase of the Krafla rifting episode 1975-1984
154 (Tryggvason 1980; Björnsson 1985; Tryggvason 1984; Passarelli et al. 2012).

155 In order to estimate the seismic potential of the HFF we assume that during the last 250 years
156 only three major earthquakes in 1755 and 1872 ruptured substantial parts of HFF. This indicates that
157 the next big event might be due soon. We furthermore assume that the stress regime on the HFF was
158 completely relaxed in the last two earthquakes of 1872 and that the slip deficit of the fault has steadily
159 increased since then.

160 **4 GPS DATA**

161 The first GPS reference markers were installed in North Iceland in 1987 to study the post-rifting relax-
162 ation after the Krafla rifting episode 1975-1984 (Foulger et al. 1992; Heki et al. 1993). This network
163 was remeasured several times in the following years (1990, 1992, 1995) to analyze the influence of
164 the rifting episode and the return to steady-state deformation (Hofton & Foulger 1996; Völksen 2000;
165 Jouanne et al. in prep.). Another, partially overlapping network was installed in 1995 to study the TFZ
166 and it has been remeasured completely five times (1997/1999/2002/2007/2010) and partially on sev-
167 eral occasions (2000/2001/2005/2009/2011), i.e. mostly the GPS markers close to Húsavík (Jouanne
168 et al. 1999, 2006, in prep.). 15 new campaign GPS points were added in 2009-2011 to improve the
169 GPS station density near the HFF. Today the TFZ GPS network consists of 14 continuous and 61
170 campaign GPS stations (Figure 1, Table 3).

171 **4.1 GPS campaigns 1997-2011**

172 During GPS campaigns, each point was typically measured for two consecutive nights, except in
173 1997, when the observation time was somewhat shorter (~ 24 hours). The GPS antennas were aligned
174 to magnetic north in the earlier campaigns, whereas in the 2009 campaign and after the antennas were
175 aligned with true north using a magnetic declination of -14 degrees. The instrument types and the

176 number of points measured differed between campaigns, see summary information in Table 1. The
177 publications by Jouanne et al. (2006, in prep.) provide more information about the acquisition strategy
178 of the 1997-2007 GPS data. In 2009 we installed four new markers on the profile across the HFF and
179 in 2010-2011 we added 11 more data points that enhance the network density North and South of the
180 on-land part of the HFF (Figure 1). The short time-series of these 15 points are not included in the
181 work we present here.

182 **4.2 Data Processing with GAMIT-GLOBK and BERNESE**

183 The entire campaign GPS data set 1997-2010 was processed independently with GAMIT-GLOBK
184 V10.4 (Herring et al. 2010a,b,c) and Bernese V5.0 (Dach et al. 2007) in order to test robustness of the
185 resulting GPS velocities. The details of the processing methods are given in Table 2. Both software
186 packages constrain daily network solutions using a well-chosen set of reference (IGS) stations. In
187 both cases we included IGS stations as well as CGPS stations in North Iceland (when available)
188 in the data analysis and we corrected for offsets in the time-series of the continuous GPS stations
189 due to earthquakes or antenna changes. We used the same ocean-loading model (FES2004), absolute
190 antenna phase center models, and the Saastamoinen model to correct for the atmospheric delay. The
191 dry/wet delay was corrected with the GMF (in GAMIT-GLOBK) and NIELL (in BERNESE) mapping
192 function. In the GAMIT processing we used a slightly higher cut-off-angle (10°) than in the BERNESE
193 processing (5°).

194 In GPS campaigns before 2009 the antennas were aligned with magnetic north instead of true
195 north. Since the antenna phase center usually does not coincide with the geometrical antenna cen-
196 ter and can deviate quite substantially, a correction to that shift should improve the results. We cor-
197 rected for this shift in the GAMIT processing but not in the BERNESE processing. In addition, during
198 GAMIT processing we already removed data outliers in the EGPS data, whereas with BERNESE
199 we processed all the EGPS data without restrictions. Therefore, the BERNESE results needed some
200 post-processing visual quality control and filtering (see last part of section 5.3).

201 **4.3 Continuous GPS data 2006-2011**

202 In addition to the episodic GPS (EGPS) data 1997-2010 we use velocities of 14 continuous GPS
203 (CGPS) stations in North Iceland plus one additional station in east Iceland (HEID). The CGPS net-
204 work was densified significantly from 4 to 14 stations in 2006 as we described in our previous study
205 (Metzger et al. 2011). In that study we estimated the velocities with a superposition of a linear trend
206 and a sinusoidal oscillation term. Here we have a better constrained estimation of the interseismic de-
207 formation rates due to an additional year of data and an improved correction of the transient volcanic

208 signal of Theistareykir volcano. We explain in the following section how we derive the interseismic
 209 deformation rates for all the GPS sites.

210 **5 ESTIMATION OF INTERSEISMIC GPS VELOCITIES**

211 Tectonic plates move steadily over millions of years but at plate boundaries the deformation is highly
 212 episodic. Most plate boundaries are locked for long periods of time and then suddenly become active
 213 in discrete events such as earthquakes or rifting episodes. The earthquake deformation cycle consists
 214 of slow but steady inter-seismic, sudden co-seismic, and transient post-seismic deformation. In rift
 215 zones as the NVZ, rifting episodes cover the average spreading of hundreds of years within relatively
 216 short rifting episodes that typically last a few years, followed by decaying post-rifting-relaxation. In
 217 addition, volcanic centers within rift zones can go through periods of inflation or deflation, which may
 218 cause transient signals in GPS time-series. In this paper we want to extract the steady-state deforma-
 219 tion rates within and around the TFZ, in particular the inter-seismic deformation rates near the HFF
 220 to constrain model parameters for the fault, so we can estimate the slip deficit of the locked HFF ac-
 221 cumulated since the last major earthquake. This means that we have to identify and eliminate possible
 222 transient signals within the GPS time-series to isolate the linear interseismic deformation rates of the
 223 TFZ.

224 The Krafla rifting episode ended 25 years ago and its effect on GPS velocities appears to have
 225 diminished before 1997 (Völksen 2000; Jouanne et al. in prep.). We therefore assume that the plate-
 226 boundary deformation rates during the observation time can be approximated as linear. On the other
 227 hand, inflation at Theistareykir central volcano 2007-2009 caused a transient deformation signal at
 228 neighboring GPS sites that we have to take into account (Metzger et al. 2011). In addition to tec-
 229 tonic signals, annual oscillation signals are visible within the continuous GPS time-series. Figure 2
 230 schematically shows the different components apparent in the acquired GPS time-series of the TFZ.
 231 We model the CGPS time-series using the following function:

$$f(t) = A + Bt + C \cos(2\pi t + \phi) + D \tan^{-1} \left(\frac{t - t_c}{t_d} \right) \quad (1)$$

232 where $A + Bt$ represents the linear displacement rate, C the amplitude and ϕ the phase shift of annual
 233 oscillations and D the amplitude, t_c the central time and t_d the curvature factor of the transient volcanic
 234 inflation at Theistareykir central volcano. In order to extract the steady interseismic velocities, we have
 235 to first correct all the GPS data for the volcanic transient signal (section 5.1) and - in case of CGPS
 236 data - annual oscillations (section 5.2).

237 5.1 Uplift at Theistareykir Volcano

238 In our previous work we detected uplift in ENVISAT interferograms at Theistareykir central volcano
239 with a maximum uplift rate of 3 cm yr^{-1} between 2007 and 2008 (Metzger et al. 2011). Using both
240 an ascending and a descending interferogram we were able to fit the spatial pattern of the inflation
241 well with a Mogi source (Mogi 1958) and thus constrain the source location. However, the limited
242 ENVISAT catalog does not contain enough data to analyze well the temporal evolution of the volcanic
243 inflation. The CGPS time-series do not provide useful information about the transient either, because
244 they started in the midst of the inflation period and the CGPS stations are located too far away from
245 the inflation center. We therefore assumed that the volcanic uplift occurred at constant rate during the
246 CGPS observation period of 2006-2010 (Metzger et al. 2011). Here we use InSAR time-series analysis
247 of ERS-1/2 satellite data to shed a better light on the uplift evolution at Theistareykir volcano.

248 We produced a number of interferograms out of 38 descending orbit scenes of the ERS-1 and 2
249 satellites spanning the time-period from 1992 until 2010 using the GAMMA software (GAMMA v1.0
250 2006). We then performed time-series analysis of the unwrapped interferograms using the π -RATE
251 software package (Poly-Interferogram Rate And Time-series Estimator, 2009) that was developed by
252 Biggs et al. (2007), Elliot et al. (2008) and Wang et al. (2009). The expected steady-state deformation,
253 i.e. due to plate spreading across the plate boundary and interseismic strain accumulation near the
254 HFF, covers the whole scene and would be partially removed by the software during the correction
255 of orbital errors. We preserve the cross-boundary signal by removing predicted line-of-sight (LOS)
256 displacements from the interferograms *before* the orbital and topographical error correction and then
257 add these predicted displacements back in again. The predicted displacements were derived from the
258 deformation model of Metzger et al. (2011). The InSAR time-series processing steps are explained in
259 more detail in Metzger & Jónsson (in prep.).

260 We extract an $800 \text{ m} \times 800 \text{ m}$ area from the InSAR time-series results, centered at Theistareykir
261 volcano, and calculate the mean LOS displacement for each image acquisition date between 1992 and
262 2010 (Figure 3). We find a linear rate between 1997 and 2007 that is caused by steady-state plate-
263 boundary processes. Sudden uplift of $\sim 78 \text{ mm}$ in line-of-sight (LOS) occurred in 2007, that seems to
264 have ended in late 2008. Before 1997 we can see another transient which was most probably caused by
265 deep magma accumulation at the Krafla volcanic system as reported by de Zeeuw-van Dalssen et al.
266 (2004).

267 We fit an inverse tangens functional to the temporal evolution of LOS displacements after 1997
268 (Figure 3):

$$f(t) = A + Bt + D_0 \tan^{-1} \left(\frac{t - t_c}{t_d} \right), \quad (2)$$

269 that is defined with amplitude D_0 , central time t_c , i.e. the time of maximum uplift rate and transient
 270 time t_d . Using a non-linear optimization routine we find central time $t_c = 2007.88$ and transient time
 271 $t_d = 0.33$ years. The total LOS displacement D_0 above the central volcano is 78 mm. If we use the
 272 Mogi source location and depth of 8.5 km derived by Metzger et al. (2011), this corresponds to a total
 273 Mogi volume change of $25 \times 10^6 \text{ m}^3$. We then use the two parameters t_c and t_d and the Mogi source
 274 to correct for the transient volcanic deformation at each GPS observation point before estimating the
 275 linear GPS velocities in sections 5.3 and 5.4.

276 5.2 Annual oscillations within CGPS time-series

277 The CGPS time-series show substantial annual oscillations, particularly in the vertical component
 278 (Grapenthin et al. 2006). After removing the volcanic uplift signal from the continuous time-series
 279 (section 5.1) we then fit the following function,

$$f(t) = A + Bt + C \cos(2\pi t + \phi) \quad (3)$$

280 with a linear velocity term $A + Bt$ and an oscillation term C to each single component and station.
 281 Before the final non-linear optimization run, outliers were removed in two separate stages: First, all
 282 data points with a standard error three times larger than the mean error were dismissed. This affected
 283 only a couple of data points. After a first optimization run we excluded also all data points with a misfit
 284 three times larger than the mean misfit. The amount of excluded data for each station-component was
 285 never larger than 4%. With a second optimization run we extracted the CGPS velocities of the cleaned
 286 data set. The resulting phase shift and amplitude parameters are plotted in Figure 4 and show clearly,
 287 how the vertical component contains the strongest oscillation signal with a maximum value in winter
 288 time ($\phi = 0$). For the East and North component the amplitude is much smaller and thus not as nicely
 289 aligned with its mean value. However it is interesting to see that the mean phase shift for the East and
 290 North components differ from the vertical component with a maximum in October and September,
 291 respectively. The average RMS values for the residuals of the time-series after removing the model
 292 described in Eq. (3) are 1.5 mm for the horizontal component and 5.1 mm for the vertical component
 293 (Fig. 5).

294 5.3 Estimation of the EGPS velocities

295 The campaign data have always been acquired during summers so we ignore possible influence from
 296 annual oscillations. After correcting the EGPS time-series for the transient volcanic signal at The-
 297 istareykir we estimate the velocity for each station-component. For the EGPS data points we get a
 298 mean standard deviation from the assumed linear model of 3.4 mm for the horizontal and 22.3 mm
 299 for the vertical components (Fig. 5). The velocity variance was scaled by $1/T^2$, where T is the total
 300 duration of each time series (Geirsson et al. 2006; Metzger et al. 2011).

301 The EGPS data set was analyzed independently with both the BERNESE V5.0 and the GAMIT-
 302 GLOBK software packages as discussed in section 4.2. To estimate the interseismic velocities of
 303 the EGPS stations we used SNX-files obtained from the BERNESE processing and the time-series
 304 resulting from the GLOBK analysis. Within GAMIT processing the data were already cleaned from
 305 potential outliers. This was not the case for the BERNESE data set where all data were processed and
 306 we therefore applied a visual quality control in the velocity estimation process to eliminate outliers in
 307 each time-series.

308 The resulting BERNESE and GAMIT velocity fields match well within uncertainties. We find that
 309 the velocities derived from GAMIT point slightly more towards the South (mean shift: 0.6 ± 0.6 mm yr⁻¹)
 310 and the East (0.3 ± 0.6 mm yr⁻¹) than the BERNESE solutions. The vertical components of GAMIT
 311 also show less upward motion (2.1 ± 1.5 mm yr⁻¹). Although this indicates a slight shift between the
 312 two network solutions we consider it as neglectable. The standard deviations of the shifts are larger
 313 than the shift itself, and what is more important, we account for a possible reference frame offset in
 314 our modeling in any case. The EGPS velocities we used in the modeling (Section 6) were obtained
 315 using the GAMIT-GLOBK software (Table 3).

316 5.4 Interseismic deformation in North Iceland

317 The estimated velocities and uncertainties for both the CGPS and EGPS stations are plotted in Figure 6
 318 in a reference frame originally based on stable North American plate (MORVEL, DeMets et al. 2010),
 319 but modified with a small offset estimated in the modeling (Section 6). This correction was necessary
 320 for the modeling as GPS points located on the North American plate, i.e. southwest of Húsavík, are not
 321 entirely stable in the North American reference frame and show a 2-4 mm yr⁻¹ motion to the northwest.
 322 A similar motion pattern has been seen in previous studies (e.g. Árnadóttir et al. 2009) and it seems
 323 to apply to all GPS stations in Northwest Iceland, indicating a local reference frame problem.

324 We find that the TFZ covers the full plate motion of 18 mm yr⁻¹ and that the deformation gradient
 325 across the NVZ is particularly strong (Figure 6). All data vectors are more or less perpendicular to the
 326 orientation of the NVZ, except for stations close to Krafla central volcano that are influenced by local

327 subsidence. Station velocities South of Skjálíandi Bay towards the Northern tip of Tjörnes Peninsula
328 gradually increase, indicating a locked Húsavík Flatey fault (see Figure 1 for geographic locations).

329 Due to potential inconsistencies of the antenna height measurements the vertical deformation rates
330 of EGPS data have to be interpreted with caution. North of Krafla central volcano a broad uplift of up
331 to 6 mm yr⁻¹ is apparent (Figure 6). This signal coincides with uplift seen in InSAR data during 1993-
332 1999 (de Zeeuw-van Dalssen et al. 2004) that was thought to be caused by deep magma accumulation
333 north of Krafla central volcano. At Krafla (relative) subsidence is visible, which is still ongoing but
334 has been slowly decaying since the end of the Krafla rifting episode (Sturkell et al. 2008).

335 **6 MODELING**

336 We describe the surface deformation of the TFZ as it has been observed by episodic and continuous
337 GPS measurements during the last 14 years with an interseismic back-slip model. This model consists
338 of a set of nine planar plate-boundary segments with a fixed (Cartesian) geometry in an elastic half-
339 space, as described by Metzger et al. (2011). The location of the plate boundary segments is shown in
340 Figure 1: The boundary follows roughly the Krafla fissure swarm in the South, then separates into two
341 sub-parallel discontinuities along the Húsavík-Flatey Fault (HFF1 and 2) and the Grímsey Oblique Rift
342 (GOR) that again reunite North of the TFZ at the Kolbeinsey Ridge. The plate-boundary deformation
343 is described by superimposing reverse slip (“back-slip”) on the locked part of the plate boundary onto
344 rigid plate motion. The model does not allow for any rotation, because the slip on each model segment
345 is uniform and is defined by the overall relative plate motion. Unlike in our previous study we do
346 not include volcanic inflation at Theistareykir in the modeling, as we already eliminated this transient
347 signal in the time-series analysis (section 5). Otherwise, the model parameter optimization and error
348 estimation procedures follow Metzger et al. (2011). The model parameter uncertainties are estimated
349 by stochastically propagating the data errors through the modeling and do therefore not include the
350 impact of model assumptions and simplifications. We here refer to this method as “error propaga-
351 tion” and compare it to a second, independent uncertainty estimation, based on Bayesian estimation
352 (section 6.1).

353 The model segments are described by 10 parameters each, but many of them are constrained
354 due to (1) the fixed location and vertical dip, (2) only two types of locking depths for the strike-slip
355 segments (HFF1/2 and GOR in Figure 1) and “rift-type” segments (all other segments), and (3) no
356 dip-slip motion. The key parameter we solve for is the locking depth of the HFF (Table 4). This value,
357 along with the fault’s length, determines the size of the locked HFF plane. Additional parameters are
358 the locking depth of the ridge segments, the partitioning of transfer motion among the two lineaments
359 HFF and GOR and the magnitude and azimuth of the overall plate spreading motion (Table 4). Two

360 auxiliary parameters allow for a small shift of the North American reference frame into a model
 361 frame, which assumes a stable reference point Southwest of the HFF. Together, the spreading vector
 362 and the partitioning of motion between the HFF and GOR define the slip-rate on the HFF. The slip-rate
 363 provides information about the stressing rate on a fault plane since the last large earthquake and gives,
 364 together with the locking-depth, an estimation of its seismic potential.

365 We include horizontal velocity components of all the CGPS and EGPS stations in the model
 366 parameter optimization (Table 3, except for one CGPS and two EGPS stations located near Krafla
 367 central volcano (MYVA/KRAF/HVIT). These stations are influenced by local subsidence at Krafla,
 368 which we do not account for in our model, because it is far from the HFF and does not influence
 369 near-fault velocities.

370 We find a locking depth for the HFF (and the GOR) of 6.2 km and 3.2 km for the ridge segments.
 371 The total relative plate motion of 20.3 mm yr^{-1} with an azimuth of 109.4°E is separated between
 372 the HFF and the GOR in a ratio of 33%/67%. The resulting data fit obtained by the best fit model
 373 parameters (Table 4) is in general very good (Figure 8, Table 3), except for the area north of Krafla
 374 central volcano where the steady-state interseismic deformation is slightly modified by uplift and
 375 extension. This is presumably due to deep magma accumulation during 1993-1999 (de Zeeuw-van
 376 Dalftsen et al. 2004).

377 6.1 Validation of the uncertainty estimation using a Bayesian estimation

378 We estimated the uncertainties of the best fit model parameters (Table 4) by analyzing outcomes of
 379 10'000 optimization runs with slightly modified (“noisy”) input data. This method of estimating pa-
 380 rameter uncertainties only considers the errors in the input data, but does not include errors from
 381 the modeling procedure or due to model simplifications. The resulting model parameter uncertainties
 382 should therefore be regarded as minimum uncertainties. Now, we validate this method of error prop-
 383 agation by applying Bayesian estimation, which provides a posterior probability distribution over the
 384 model parameters given the recorded data and serves as an independent assessment of the model.

385 We assume a linear M -dimensional model space \mathcal{M} , and a linear D -dimensional data space \mathcal{D} . The
 386 forward operator between these two spaces g , is assumed to be only mildly nonlinear. The recorded
 387 measurements \mathbf{d} and model parameters \mathbf{m} are assumed to be realizations of the random variables D
 388 and M such that

$$\mathbf{d} = g(\mathbf{m}) + \epsilon, \quad (4)$$

where ϵ is a realization of stochastic noise. The posterior density in the model space is calculated according to Bayes' formula, here given in the form of Tarantola (2005)

$$\sigma_{\mathcal{M}}(\mathbf{m}) = kL(\mathbf{m}) \rho_{\mathcal{M}}(\mathbf{m}), \quad (5)$$

where k serves as a normalization constant and $\rho_{\mathcal{M}}(\mathbf{m})$ represents the prior beliefs held of the parameters. The prior was chosen to be separately uniform distributions on every parameter m_i between two physically chosen bounding values $m_i^{\min} < m_i < m_i^{\max}$. The likelihood function

$$L(\mathbf{m}) = \int_{\mathcal{D}} \rho_{\mathcal{D}} \theta(\mathbf{d}|\mathbf{m}) \, d\mathbf{d} \quad (6)$$

gives a measure of how good a model \mathbf{m} is for explaining the data. $\rho_{\mathcal{D}}$ is the prior information on the data, and $\theta(\mathbf{d}|\mathbf{m})$ represents the correlation between the data and model parameters. Assuming the theoretical relationship between model parameters and data to be exact, $\theta(\mathbf{d}|\mathbf{m}) = \delta(\mathbf{d} - g(\mathbf{m}))$, allows to solve equation 5. From the independence of ϵ and \mathbf{m} in equation 4, and from the assumption of Gaussian errors it follows that (Tarantola 2005)

$$\sigma_{\mathcal{M}} \propto \rho_{\mathcal{M}}(\mathbf{m}) \exp\left(-\frac{1}{2}(\mathbf{d} - g(\mathbf{m}))^T \Sigma^{-1}(\mathbf{d} - g(\mathbf{m}))\right) \quad (7)$$

This density $\sigma_{\mathcal{M}}$ must then be evaluated by a Markov Chain Monte Carlo (MCMC) method due to the high dimensionality of model space \mathcal{M} . An MCMC algorithm is an algorithm for constructing a Markov chain with an equilibrium distribution equal to a given probability density function. The Metropolis-Hastings (M-H) algorithm (Hastings 1970) is an MCMC algorithm that picks the following state from a proposal distribution that is simpler than the sampled distribution, but uses a condition for rejecting unlikely states with greater probability to more likely ones. To find suitable parameters for this proposal distribution we first used a parameter-free MCMC algorithm called the Gibbs sampler described in (Geman & Geman 1984). The Gibbs sampler iteratively samples the conditional distributions of each variable, making it considerably slower for the problem at hand that lacks simple conditional distributions.

The M-H algorithm was started as multiple chains from arbitrary non-zero starting points in the model space. The first third of every chain is discarded to ensure convergence. The remaining samples are treated for auto-correlation by thinning, where only every τ^{th} sample was picked, so that samples τ steps apart are uncorrelated. τ was determined by the Geyer IMSE heuristic described in Geyer (1992). The remaining samples were considered representative of the posterior density (Eq. 7).

The resulting marginal distributions of the model parameters from the Bayesian estimation are in a perfect agreement with the uncertainty estimation obtained by the error propagation (Figure 7).

416 Since one Bayesian estimation needs much less calculation time than obtaining a significant statistic
417 from the error propagation method, we compare the 10'000 optimization runs of the error propagation
418 method with one million of samples from the Bayesian estimation. This explains the difference in
419 smoothness of the marginal distributions in Figure 7. The 68%- and 95%-confidence levels do not
420 deviate from each other more than 2% for any parameters. This result is reassuring and confirms the
421 validity of the error propagation method for determining the part of the model parameter uncertainties
422 that is caused by errors in the input data.

423 7 DISCUSSION

424 The kinematic model presented in this paper is based on GPS time-series from 14 continuous GPS
425 stations running since 2006 and 44 GPS markers that have been remeasured at least five times since
426 1997. We can compare the obtained result directly to our previous results (Metzger et al. 2011) where
427 we used only the 14 CGPS data points (Tab. 4). The CGPS stations lie primarily on a profile across the
428 two lineaments HFF and GOR and are sparse near the volcanic rift zone, which previously resulted
429 in a poorly constrained ridge locking depth. The campaign GPS observations complement the CGPS
430 network nicely and fill the gaps in the Northern Volcanic Zone and on the Flateyarskagi peninsula
431 Southwest of the HFF (Fig. 1). This is the reason why the uncertainties of all our model parameters
432 are at least 50% smaller (Tab. 4) and why we get significant changes for the locking depth of the ridge
433 segments (from 4.8 to 3.2 km) and for the azimuth of plate motion (from 115°E to 109.4°E), which
434 is now closer to the MORVEL plate motion azimuth of 105°E. The full plate motion increases again
435 slightly from our previous best-fit estimate of 19.6 to 20.3 mm yr⁻¹, which might be due to the broad
436 uplift signal north of Krafla central volcano (Fig. 8) that also influences the horizontal displacement
437 rates. All other parameters express only a slight change within or close to the uncertainty limits of our
438 last study.

439 However, thanks to the improved data set, the estimated model parameter uncertainties have be-
440 come so small that model uncertainties, which are not assessed in this study, would probably outweigh
441 the propagated data uncertainties. In other words, if we use a different geometry for the plate bound-
442 ary segments or another Earth model than an elastic half-space, the estimated model parameters would
443 likely change beyond the current model parameter confidence bounds. Therefore, the estimated model
444 parameter uncertainties should be regarded as minimum uncertainties as they only include the effect
445 of the data errors. Further important model assumptions are: A complete stress release in 1872 when
446 the last large earthquakes hit the HFF, a steady stress accumulation since then and a constant locking
447 depth along the HFF segments. This last simplifying assumption is needed as the locking depth is
448 mostly constrained by data points close to the Southeastern end of the HFF, leaving no control over

449 the Northwestern part of the fault. Finally, we do not know exactly the effect of the Krafla rifting
450 episode on the stress-regime of the HFF. Coulomb failure stress calculations derived from an opening
451 dyke model at Krafla suggest a stress drop on the eastern part of the HFF, which might have relieved
452 some of the accumulated stress on the fault (Maccaferri et al. 2012).

453 In comparison to our previous study, the implications on the seismic potential of the HFF fault
454 do not change much and are in the same range of the 1755 and 1872 earthquakes. The slightly faster
455 slip rate is neutralized by a slightly lower locking depth. To put the obtained modeling results in a
456 general context, Table 4 compares the results of previous studies that provide information about the
457 locking depth and slip rate of the HFF. Some of these studies are based in part on the same CGPS and
458 EGPS data we use in this paper, while others are based on geological information (Sæmundsson 1974),
459 seismicity analysis (Rögnvaldsson et al. 1998) or ISNET campaign GPS data (Árnadóttir et al. 2009).
460 All these studies generally agree on the slip rate and locking depth of the HFF. A notable exception
461 is the locking depth inferred from the results of Rögnvaldsson et al. (1998) that is almost twice as
462 large as the estimates based on geodetic data (Metzger et al. 2011, and this study). The estimate
463 from Rögnvaldsson et al. (1998) is deduced from relocated earthquakes with most of the epicenters
464 close to the Northwestern end of the HFF while the geodetically-derived depths were constrained
465 primarily by data points located near the Southeastern end of the fault. The temperature gradient in
466 Iceland can reach $150\text{-}200^\circ\text{C km}^{-1}$ at the flanks of the rift zone and decreases to $40\text{-}50^\circ\text{C km}^{-1}$ in the
467 oldest crust in East and West Iceland (Palmason & Sæmundsson 1979). This means that the Eastern
468 end of the HFF that links to the Northern Volcanic Zone likely has a higher temperature gradient
469 than the Western, offshore end of the fault. Furthermore the seismic activity in Icelandic crust ceases
470 at temperatures above $600\text{-}800^\circ\text{C}$ and the crust becomes partially molten at 1200°C (Flóvenz &
471 Sæmundsson 1993; Björnsson 2006). A map showing the estimated depth to the 1200°C -isotherm in
472 Iceland published in Flóvenz & Sæmundsson (1993) indicates increasing isotherm depth along the
473 HFF from less than 15 km close to the triple junction at Theistareykir central volcano to more than
474 20 km at the Northwestern end of the fault. The same applies for the heat flow that decreases from
475 $140\text{-}175\text{ mW m}^{-2}$, measured in boreholes close to the Eastern end of the HFF in the Theistareykir area,
476 to 80 mW m^{-2} on Flatey island. Assuming linear temperature gradient with depth, this would result in
477 a variable thickness of the seismogenic zone and locking depth along the fault.

478 To calculate the seismic potential of the HFF we combine the fault slip-rate, length and locking
479 depth of the HFF, which results in a tightly constrained moment that corresponds to a $M_w 6.81 \pm 0.04$
480 earthquake. The model segment of the HFF is connected to the Krafla rift segment but in reality the
481 fault is ~ 20 km shorter and ends in the Theistareykir fissure swarm (Figure 1). As the seismic potential
482 scales with the size of the fault plane and the accumulated slip (Aki 1966; Hanks & Kanamori 1979),

483 the shorter fault length reduces the seismic potential by 20% to $M_w 6.75$. On the other hand, if the
484 locking depth is not uniform along the fault as our model assumes, but increases from 6.2 km in the
485 East to 12 km in the West Rögnvaldsson et al. (1998), the fault loading increases by 15% and the
486 seismic potential becomes $M_w 6.85$. Given this variability, we therefore adjust the estimated seismic
487 potential and its uncertainty to $M_w 6.8 \pm 0.1$.

488 8 CONCLUSIONS

489 The key objective of the work presented in this study was to derive a kinematic model of the Tjörnes
490 Fracture Zone in North Iceland in order to estimate the locking depth and slip deficit of the Húsavík-
491 Flatey fault (HFF), and thus its seismic potential that has accumulated since the last large earthquakes
492 in 1872. In our former paper we used only 14 CGPS stations to constrain parameters of an interseis-
493 mic back-slip model of the plate boundary in North Iceland (Metzger et al. 2011). In this paper we
494 almost quadruple the number of input GPS velocities by adding EGPS data dating back to 1997 and
495 find similar optimal model parameters while all model parameter uncertainties are reduced by more
496 than 50%. We confirm our uncertainty estimations based on data error propagation with a Bayesian
497 estimation. However, with the increased input data density, the derived model parameter uncertainties
498 have become so small that the ambiguity caused by the choice of the model would probably outweigh
499 the propagated data uncertainties and would likely significantly increase the overall model parameter
500 uncertainties. Compared to our earlier study we find a slightly larger slip-rate and a slightly shallower
501 locking depth of the HFF, resulting in an unchanged accumulated seismic moment, corresponding to
502 a $M_w 6.8 \pm 0.1$ earthquake.

503 All model parameters, except for the ridge locking depth, changed within the estimated uncertain-
504 ties. Relocated off-shore earthquakes along the western half of the HFF (Rögnvaldsson et al. 1998)
505 suggest deeper locking (10-12 km) than what we obtain from on-land geodetic data near the eastern
506 end of the fault (6.2 km). This possible along-strike variation in locking depth is supported by signifi-
507 cant change in thermal gradient along the fault from a high gradient of 80°C km^{-1} near the NVZ in the
508 east to probably $\sim 50^\circ\text{C km}^{-1}$ in the west. If the locking depth increases gradually from 6.2 km in the
509 east to 12 km in the west, it would mean that the accumulated stress is $\sim 15\%$ higher than estimated
510 above, or equivalent to a $M_w 6.85$ earthquake.

511 ACKNOWLEDGMENTS

512 The collection of EGPS data up to 2007 was conducted by Thierry Villemin and François Jouanne,
513 with financial support of the French Polar Institute IPEV (Program 316). IPEV also supported the

514 installation of the CGPS stations at Arholt (ARHO) and Raufarhöfn (RHOF). François Jouanne pro-
 515 cessed the EGPS data with BERNESE and Sigrún Hreinsdóttir helped with the GAMIT processing.
 516 Gillis Danielsen developed the codes for the Bayesian estimation. Pascale Bascou, André Blanchard,
 517 Olivier Cavalié, Gillis Danielsen, Janik Deutscher, Alice Gabriel, Notker Metzger and Rob Smith
 518 assisted in the GPS campaigns 2007-2011. The Húsavík Academic Center allowed us to use their fa-
 519 cilities during field work. Some figures were produced with the GMT public domain software (Wessel
 520 & Smith 1998).

521 REFERENCES

- 522 Aki, K., 1966. Generation and Propagation of G Waves from the Niigata Earthquake of June 16, 1964. Part 2.
 523 Estimation of earthquake moment, released energy and stress-strain drop from the G wave spectrum, *Bull. of*
 524 *the Earth. Res. Inst.*, **44**, 73–88.
- 525 Árnadóttir, T., Lund, B., Jiang, W., Geirsson, H., Björnsson, H., Einarsson, P., & Sigurdsson, T., 2009. Glacial
 526 rebound and plate spreading: results from the first countrywide GPS observations in Iceland, *Geophys. J. Int.*,
 527 **177**(2), 691–716.
- 528 Biggs, J., Wright, T., Lu, Z., & Parsons, B., 2007. Multi-interferogram method for measuring interseismic
 529 deformation: Denali Fault, Alaska, *Geophys. J. Int.*, **170**, 1165–1179.
- 530 Björnsson, A., 1985. Dynamics of crustal rifting in NE Iceland, *J. Geophys. Res.*, **90**(NB12), 151–162.
- 531 Björnsson, A., 2006. Temperature of the Icelandic crust: Inferred from electrical conductivity, temperature
 532 surface gradient, and maximum depth of earthquakes, *Tectonophysics*, **447**(1-4), 136–141.
- 533 Dach, R., Hugentobler, U., Fridez, P., & Meindl, M., 2007. *Bernese GPS Software Version 5.0*, Stämpfli
 534 Publications AG, Bern.
- 535 de Zeeuw-van Dalssen, E., Pedersen, R., Sigmundsson, F., & Pagli, C., 2004. Satellite radar interferometry
 536 1993–1999 suggests deep accumulation of magma near the crust-mantle boundary at the Krafla volcanic
 537 system, Iceland, *Geophys. Res. Lett.*, **31**(13), 5–9.
- 538 DeMets, C., Gordon, R. G., & Argus, D. F., 2010. Geologically current plate motions, *Geophys. J. Int.*, **181**(1),
 539 1–80.
- 540 Einarsson, P., 1991. Earthquakes and present-day tectonism in Iceland, *Tectonophysics*, **189**(1-4), 261–279.
- 541 Einarsson, P. & Sæmundsson, K., 1987. Earthquakes epicenters 1982-1985 and volcanic systems in Iceland, in
 542 *Í hlutarins edli, Map accompanying Festschrift for T. Sigurgeirsson*, edited by T.I. Sigfusson, Menningarssjodur,
 543 Reykjavik, Iceland.
- 544 Elliot, J., Biggs, J., Parsons, B., & Wright, T., 2008. InSAR slip rate determination on the Altyn Tagh
 545 Fault, northern Tibet, in the presence of topographically correlated atmospheric delays, *Geophys. Res. Lett.*,
 546 **35**(L12309).
- 547 Flóvenz, O. G. & Sæmundsson, K., 1993. Heat flow and geothermal processes in Iceland, *Tectonophysics*,
 548 **225**(1-2), 123–138.

- 549 Foulger, G. R., Jahn, C. H., Seeber, G., Einarsson, P., Julian, B. R., & Heki, K., 1992. Post-rifting stress-
550 relaxation at the divergent plate boundary in Northeast Iceland, *Nature*, **358**(6386), 488–490.
- 551 GAMMA v1.0, 2006. GAMMA Software Introduction, GAMMA Remote Sensing research and Consulting
552 AG, Gümligen, Switzerland, <http://www.gamma-rs.ch>.
- 553 Geirsson, H., Árnadóttir, T., Völksen, C., Jiang, W., Sturkell, E., Villemin, T., Einarsson, P., Sigmundsson, F.,
554 & Stefansson, R., 2006. Current plate movements across the Mid-Atlantic Ridge determined from 5 years of
555 continuous GPS measurements in Iceland, *J. Geophys. Res.*, **111**(B09407).
- 556 Geman, S. & Geman, D., 1984. Stochastic relaxation, Gibbs distributions, and the Bayesian restoration of
557 images, *IEEE Trans. Pattern Anal. Machine Intelligence*, **6**, 721–741.
- 558 Geyer, C. J., 1992. Practical Markov Chain Monte Carlo, *Statistical Science*, pp. 473–511.
- 559 Grapenthin, R., Sigmundsson, F., Geirsson, H., Árnadóttir, T., & Pinel, V., 2006. Icelandic rhythmicity: Annual
560 modulation of land elevation and plate spreading by snow load, *Geophys. Res. Lett.*, **33**(L24305).
- 561 Gudmundsson, A., Brynjólfsson, S., & Jonsson, M. T., 1993. Structural analysis of a transform fault-rift zone
562 junction in North Iceland, *Tectonophysics*, **220**, 205–221.
- 563 Halldórsson, P., 2005. Jarðskjálftavirkni á Norðurlandi - Earthquake activity in N-Iceland. Greinarger
564 Veðurstofu Íslands, *IMO report 05021 (in Icelandic)*, pp. 34–.
- 565 Hanks, T. C. & Kanamori, H., 1979. Moment magnitude scale, *J. Geophys. Res.*, **84**(NB5), 2348–2350.
- 566 Hastings, W. K., 1970. Monte Carlo sampling methods using Markov chains and their applications, *Biometrika*,
567 **57**(1), 97–109.
- 568 Heki, K., Foulger, G. R., Julian, B. R., & Jahn, C. H., 1993. Plate dynamics near divergent boundaries -
569 geophysical implications of postrifting crustal deformation in NE Iceland, *J. Geophys. Res.*, **98**(B8), 14279–
570 14297.
- 571 Herring, T. A., King, R. W., & McClusky, S. C., 2010a. Introduction to GAMIT/GLOBK, Release 10.4,
572 *Department of Earth, Atmospheric, and Planetary Sciences, Massachusetts Institute of Technology*.
- 573 Herring, T. A., King, R. W., & McClusky, S. C., 2010b. GAMIT Reference Manual - GPS Analysis at MIT,
574 Release 10.4, *Department of Earth, Atmospheric, and Planetary Sciences, Massachusetts Institute of Tech-*
575 *nology*.
- 576 Herring, T. A., King, R. W., & McClusky, S. C., 2010c. GLOBK Reference Manual - Global Kalman filter
577 VLBI and GPS analysis program, Release 10.4, *Department of Earth, Atmospheric, and Planetary Sciences,*
578 *Massachusetts Institute of Technology*.
- 579 Hofton, M. A. & Foulger, G. R., 1996. Postrifting anelastic deformation around the spreading plate bound-
580 ary, North Iceland. 1. Modeling of the 1987-1992 deformation field using a viscoelastic earth structure, *J.*
581 *Geophys. Res.*, **101**(B11), 25403–25421.
- 582 Homberg, C., Bergerat, F., Angelier, J., & Garcia, S., 2010. Fault interaction and stresses along broad oceanic
583 transform zone: Tjörnes Fracture Zone, north Iceland, *Tectonics*, **29**(TC1002).
- 584 INMH, 1998. Tectonic Map of Iceland, in *Icelandic Institute of Natural History*, compiled by H. Jóhannesson
585 and K. Sæmundsson, edited by Mál og menning, Reykjavík.

- 586 Jouanne, F., Villedien, T., Ferber, V., Maveyraud, C., Ammann, J., Henriot, O., & Got, J. L., 1999. Seismic risk
587 at the rift-transform junction in north Iceland, *Geophys. Res. Lett.*, **26**(24), 3689–3692.
- 588 Jouanne, F., Villedien, T., Berger, A., & Henriot, O., 2006. Rift-transform junction in North Iceland: rigid
589 blocks and narrow accommodation zones revealed by GPS 1997-1999-2002, *Geophys. J. Int.*, **167**(3), 1439–
590 1446.
- 591 Jouanne, F., Villedien, V., & Bascou, P., in prep. Current deformation of northern Iceland: Strain accumulation
592 along active faults.
- 593 Maccaferri, F., Rivalta, E., Passarelli, L., & Jónsson, S., 2012. The stress shadow induced by the 1975-1984
594 Krafla rifting episode, *subm. to JGR*.
- 595 Magnúsdóttir, S. & Brandsdóttir, B., 2011. Tectonics of the Þeistareykir fissure swarm, *Jökull*, **61**, 65–79.
- 596 McMaster, R. L., Schilling, J. G. E., & Pinet, P. R., 1977. Plate boundary within Tjörnes Fracture Zone on
597 northern Iceland's insular margin, *Nature*, **269**(5630), 663–668.
- 598 Metzger, S. & Jónsson, S., in prep. InSAR Time-Series Analysis of the Tjörnes Fracture Zone 1992-2010.
- 599 Metzger, S., Jónsson, S., & Geirsson, H., 2011. Locking depth and slip-rate of the Húsavík Flatey fault, North
600 Iceland, derived from continuous GPS data 2006-2010, *Geophys. J. Int.*, **187**(2), 564–576.
- 601 Mogi, K., 1958. Relations between the Eruptions of Various Volcanoes and the Deformations of the Ground
602 Surfaces around them, *Bull. Earthquake Res. Inst., Univ. Tokyo*, **36**, 99–134.
- 603 Palmason, G. & Sæmundsson, K., 1979. *Cermak, Rybach (Eds.), Terrestrial heat flow in Europe*, chap. Sum-
604 mary of heat flow in Iceland, Springer, Berlin, Heidelberg.
- 605 Passarelli, L., Maccaferri, F., Rivalta, E., Dahm, T., & Boku, E., 2012. A probabilistic approach for the
606 classification of earthquakes as "triggered" or "not triggered": Application to the 13th Jan 1976 Kópasker
607 Earthquake on the Tjörnes Fracture Zone, Iceland, *J. Seismol.*, **1383-4649**, 1–23.
- 608 Poly-Interferogram Rate And Time-series Estimator,, 2009. V2.0b2, [http://homepages.see.leeds.ac.
609 uk/~earhw/pirate/](http://homepages.see.leeds.ac.uk/~earhw/pirate/).
- 610 Rögnvaldsson, S. T., Gudmundsson, A., & Slunga, R., 1998. Seismotectonic analysis of the Tjörnes Fracture
611 Zone, an active transform fault in north Iceland, *J. Geophys. Res.*, **103**(B12), 30117–30129.
- 612 Sæmundsson, K., 1974. Evolution of the Axial Rifting Zone in Northern Iceland and the Tjörnes Fracture
613 Zone, *Geol. Soc. of America Bull.*, **85**, 495–504.
- 614 Sigurdsson, H. & Sparks, R. S. J., 1978. Rifting Episode in North Iceland in 1874-1875 and the Eruptions of
615 Askja and Sveinagja, *Bull. Volcanol.*, **41**(3).
- 616 Stefánsson, R., Gudmundsson, G. B., & Halldórsson, P., 2008. Tjörnes fracture zone. New and old seismic
617 evidences for the link between the North Iceland rift zone and the Mid-Atlantic ridge, *Tectonophysics*, **447**(1-
618 4), 117–126.
- 619 Sturkell, E., Sigmundsson, F., Geirsson, H., Ólafsson, H., & Theodórsson, T., 2008. Multiple volcano defor-
620 mation sources in a post-rifting period: 1989–2005 behaviour of Krafla, Iceland constrained by levelling, tilt
621 and GPS observations, *J. Volcanol. Geotherm. Res.*, **177**(2), 405–417.
- 622 Tarantola, A., 2005. *Inverse Problem Theory and Methods for Model Parameter Estimation*, Society for

- 623 Industrial and Applied Mathematics.
- 624 Thorgeirsson, O., 2012. Sögulegir jarðskáftar á Norðurlandi - Historic Earthquakes in North Iceland (in
625 Icelandic), *University of Iceland*, p. 80.
- 626 Thoroddsen, T., 1880. An Account of Volcanic Eruptions and Earthquakes which have taken place in Iceland
627 within Historical Times, *Geological Magazine*, **7**(10), 458–467.
- 628 Thoroddsen, T., 1925. Die Geschichte der isländischen Vulkane, *D. Kgl. Danske Vidensk. Selsk. Skrifter*,
629 *Naturvidensk. og Mathem. Afd.*, **8**(9), 1–458.
- 630 Tryggvason, E., 1980. Subsidence events in the Krafla area, North-Iceland, 1975-1979, *J. of Geophys.*, **47**(1-3),
631 141–153.
- 632 Tryggvason, E., 1984. Widening of the Krafla fissure swarm during the 1975-1981 volcano-tectonic episode,
633 *Bull. of Volc.*, **47**, 47–69.
- 634 Tryggvason, E., 1994. Surface deformation at the Krafla volcano, North Iceland, 1982-1992, *Bull. of Volc.*, **56**,
635 98–107.
- 636 Völksen, C., 2000. *Die Nutzung von GPS für die Deformationsanalyse in regionalen Netzen am Beispiel Is-*
637 *lands*, Ph.D. thesis, Wissenschaftliche Arbeiten der Fachrichtung Vermessungswesen, Universität Hannover.
- 638 Wang, H., Wright, T., & Biggs, J., 2009. Interseismic slip rate of the northwestern Zianshuihe fault from
639 InSAR data, *Geophys. Res. Lett.*, **36**(L03302).
- 640 Wesnousky, S. G., 1986. Earthquakes, quaternary faults, and seismic hazard in California, *J. Geophys. Res.*,
641 **91**(B12), 2587–2631.
- 642 Wessel, P. & Smith, H. F., 1998. New improved version of the Generic Mapping Tools released, *EOS Trans.*
643 *Am. Geophys. Un.*, **79**(47), 579.

Table 1. Information about the GPS campaigns 1997-2011, including the number of instruments (sets) and the number of measured points (pts). All campaigns were carried out between July and September of the given year.

Year	Receiver type	Antenna type	sets	pts
1997	ASHTECH Z-XII3	ASH700718B/D	7	45
1999	ASHTECH Z-XII3	ASH700936B_M	4	45
	ASHTECH UZ-12		4	
2002	ASHTECH Z-XII3	ASH700936A_M	5	46
	ASHTECH UZ-12		5	
2005	ASHTECH UZ-12	ASH700936A_M		16
2007	ASHTECH UZ-12	TRM41249.00	13	40
2009	TRIMBLE NETRS	TRM41249.00	2	8
	LEICA SR530	LEIAT502	2	8
2010	ASHTECH UZ-12	TRM41249.00	10	51
2011	TRIMBLE NETR9	TRM57971.00	6	23

Table 2. Details of the GPS processing with the GAMIT-GLOBK v10.4 (Herring et al. 2010a,b,c) and Bernese V5.0 (Dach et al. 2007) software.

	GAMIT-GLOBK	BERNESE
Reference stations (IGS)	max. 19	max. 10
Reference frame	ITRF 2005	ITRF 2005
Orbits/Clock files	IGS	IGS
Antenna model	Abs. phase center	Abs. phase center
Tropospheric corr.	Saastamoinen	Saastamoinen
Dry/Wet delay mapping	GMF	NIELL
Ocean loading model	FES2004	FES2004
Cut-off-angle	10°	5°
Offset correction	Yes	Yes
Magnetic North	Yes	No (until 2007)

Table 3. Station abbreviations, coordinates, observed and modeled GPS velocities from continuous GPS stations 2006-2011 (upper part) and from EGPS data from 1997-2010 (lower part). The velocities are corrected for the volcanic uplift transient at Theistareykir in 2007-2009 and seasonal oscillation (Section 5) and represent the interseismic plate-boundary deformation. The reference frame is based on stable North America (MORVEL, DeMets et al. 2010) but slightly modified using an auxiliary model parameter (Section 6).

Station abbreviation	Latitude [°N]	Longitude [°W]	Observed velocities			Modeled velocities	
			East [mm/yr]	North [mm/yr]	Up [mm/yr]	East [mm/yr]	North [mm/yr]
AKUR	65.68543	18.12248	1.7±0.3	0.4±0.3	3.9±1.0	0.8	-0.2
ARHO	66.19307	17.10904	8.5±0.2	-4.0±0.3	0.0±0.7	7.6	-2.8
FTEY	66.16032	17.84792	4.6±0.3	-1.0±0.3	-0.3±1.1	4.7	-1.6
GAKE	66.07809	16.76466	11.5±0.3	-3.9±0.4	2.0±1.2	9.9	-4.0
GMEY	66.53897	18.01901	7.6±0.2	-3.9±0.2	-2.9±1.1	8.5	-2.1
GRAN	65.91866	17.57861	1.1±0.4	-0.1±0.3	3.0±1.2	1.6	-0.5
HEDI	66.08072	17.30945	5.3±0.3	-1.4±0.3	1.3±1.1	5.7	-2.3
HEID	65.38085	14.54095	19.3±0.3	-8.5±0.3	4.3±0.9	18.8	-6.7
HOTJ	66.16166	17.24426	7.2±0.3	-3.0±0.3	-0.1±1.1	6.9	-2.6
KOSK	66.30325	16.44343	16.0±0.4	-7.6±0.5	2.3±1.1	16.5	-7.4
KVIS	66.10075	17.27171	5.8±0.3	-2.6±0.3	0.2±1.0	6.2	-2.5
MYVA	65.64232	16.89135	11.5±0.2	0.4±0.3	1.0±0.9	-	-
RHOF	66.46112	15.94671	17.3±0.2	-7.9±0.2	0.5±0.9	18.3	-6.9
SAVI	65.99319	17.37610	1.6±0.3	-0.5±0.3	2.2±1.2	3.0	-0.9
SIFJ	66.13804	18.89935	1.8±0.3	-2.0±0.3	-2.2±1.1	1.0	0.1
ADDA	65.87335	17.36474	1.6±0.2	0.5±0.2	3.2±3.7	1.9	-0.6
AEDA	65.98403	17.41486	2.2±0.2	-0.7±0.4	-0.5±1.9	2.6	-0.8
AUDB	66.09650	16.95311	6.9±0.3	-3.6±0.4	1.3±1.7	7.6	-3.1
AUSB	65.71412	16.53632	16.7±0.3	-6.0±0.3	7.1±1.9	16.1	-6.2
BAKH	66.07600	17.35812	4.9±0.4	-1.7±0.4	0.1±2.0	5.3	-2.1
BANG	66.14436	16.96801	7.6±0.2	-4.0±0.2	-3.0±2.9	7.7	-3.1
BAUS	66.03179	17.25267	4.7±0.2	-2.2±0.4	0.8±2.0	4.8	-1.9
BLAS	65.96293	16.87685	7.4±0.3	-2.7±0.2	4.8±2.2	7.4	-3.2
BREV	66.19273	17.13735	8.0±0.3	-3.3±0.3	-0.1±1.7	7.5	-2.7
FLAD	66.10728	17.89832	2.9±0.2	-0.5±0.2	-3.3±1.7	2.8	-0.7
FLAT	66.15807	17.85308	4.7±0.4	-0.8±0.2	-4.0±1.9	4.6	-1.5
GAUR	66.08112	16.77020	11.0±0.3	-4.1±0.2	-0.5±1.8	9.8	-3.9
GEIR	65.89674	17.56457	1.6±0.4	0.1±0.3	0.0±2.7	1.6	-0.5
GREN	65.97315	18.22341	1.1±0.2	-0.8±0.4	-0.9±2.2	1.0	-0.2
HAHN	66.44703	16.46671	16.5±0.2	-7.7±0.3	-2.0±1.7	17.7	-7.0
HAMH	65.85531	17.05957	2.1±0.3	0.5±0.3	3.0±1.5	3.2	-1.2
HAST	65.92881	16.44621	18.4±0.3	-5.5±0.3	5.5±1.4	16.3	-6.6
HAUG	65.93853	18.33757	1.6±0.2	-0.3±0.2	-0.2±1.4	0.9	-0.1
HEHO	66.04866	16.95689	6.5±0.3	-3.3±0.2	2.9±2.9	7.3	-3.1

Table 4. The best fit model parameters in comparison to the results of previous studies. The fault-parallel slip rate along the two HFF segments (Figure 1) is derived from the partial transform motion parameter and the parameter describing amplitude and azimuth of the relative plate motion. The studies denoted with an asterisk (*) share parts of the data set.

Data type	CGPS/EGPS* ¹⁾	CGPS* ²⁾	CGPS* ³⁾	EGPS* ⁴⁾	EGPS* ⁵⁾	InSAR ⁶⁾	Seismicity ⁷⁾	Geology ⁸⁾
Acquisition period	1997-2011	2006-2010	2001-2004	1993-2004	1997-2002	1993-1999	1994-1998	7-9 Myr
Locking depth HFF [km]	$6.2^{+0.8}_{-0.7}$	$6.3^{+1.7}_{-1.2}$		4-15	>10-12		10-12	
Partial motion HFF [%]	33.4 ± 1.4	$33.9^{+3.1}_{-3.2}$	40					
Slip HFF1 [mm/yr]	6.8 ± 0.3	$6.6^{+0.7}_{-0.6}$	~7	<5	~8			<7-8
Slip HFF2 [mm/yr]	6.6 ± 0.3	$6.6^{+0.7}_{-0.6}$	~7	<5	~8			<7-8
Locking depth Ridge [km]	3.2 ± 0.2	$4.8^{+1.6}_{-1.1}$		5±2		4.6		
Plate spreading [mm/yr]	$20.3^{+0.4}_{-0.3}$	$19.6^{+0.8}_{-0.6}$		23±2		25-34		
Spreading azimuth [°E]	109.4 ± 0.7	$115.1^{+1.2}_{-1.6}$						
Mogi volume [10^6m^3]	25	$9.4^{+1.2}_{-1.0}$						
¹⁾ This study	³⁾ Geirsson et al. (2006)	⁵⁾ Jouanne et al. (2006)				⁷⁾ Rögnvaldsson et al. (1998)		
²⁾ Metzger et al. (2011)	⁴⁾ Árnadóttir et al. (2009)	⁶⁾ de Zeeuw-van Dalssen et al. (2004)				⁸⁾ Sæmundsson (1974)		

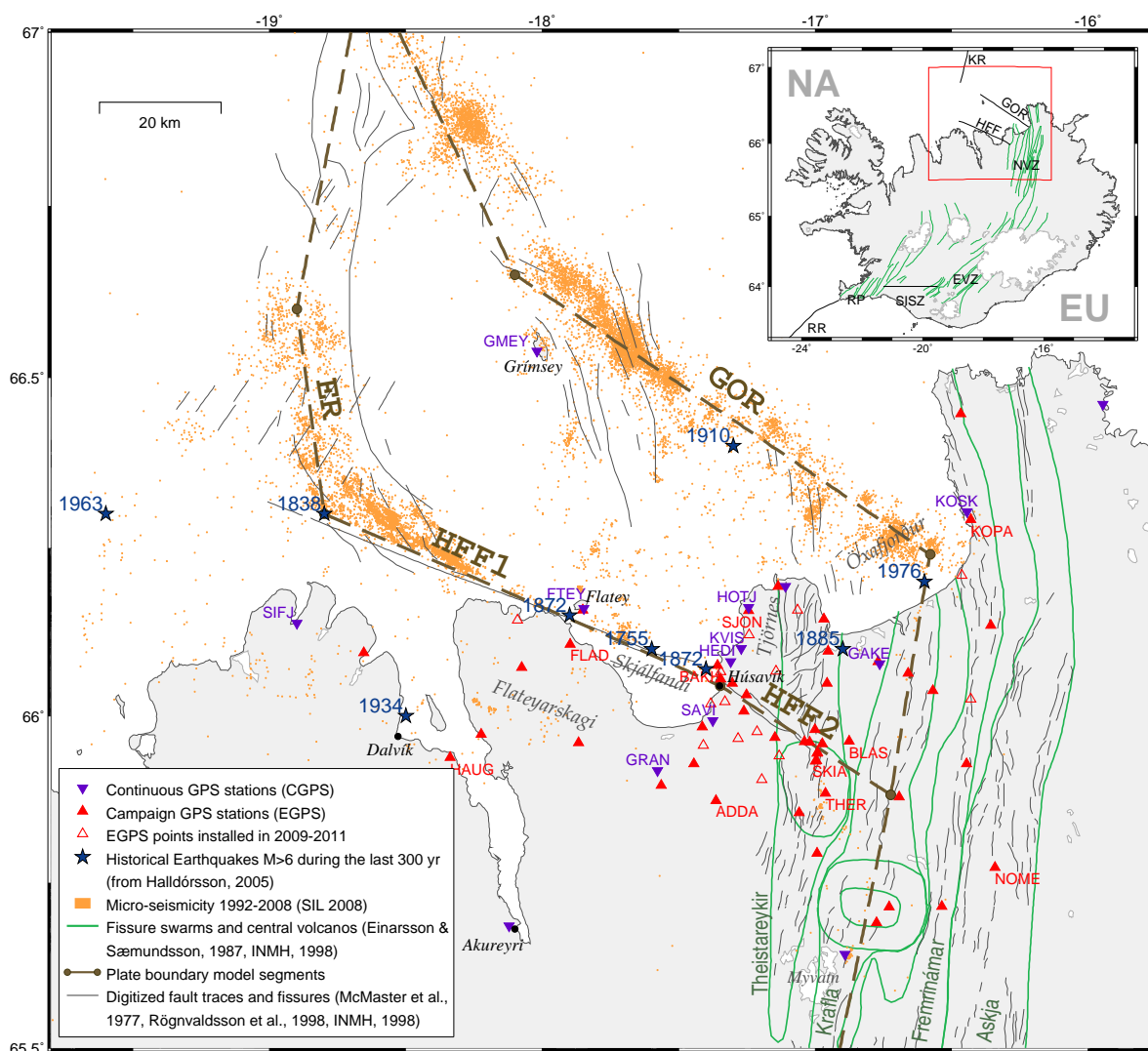


Figure 1. Tectonic setting, seismicity and GPS markers in North Iceland. The mid-Atlantic Ridge separates the North American (NA) and the Eurasian plate (EU) and is offset by the South Icelandic Seismic Zone in the South (SISZ) and by the Húsavík-Flatey Fault (HFF) and the Grímsey Oblique Rift (GOR) in the North (inset). Other plate boundary segments: ER – Eyjafjarðaráll Rift, EVZ – Eastern Volcanic Zone, KR – Kolbeinsey Ridge, NVZ – Northern Volcanic Zone, RP – Reykjanes Peninsula, RR – Reykjanes Ridge. The station labels refer to Fig. 5.

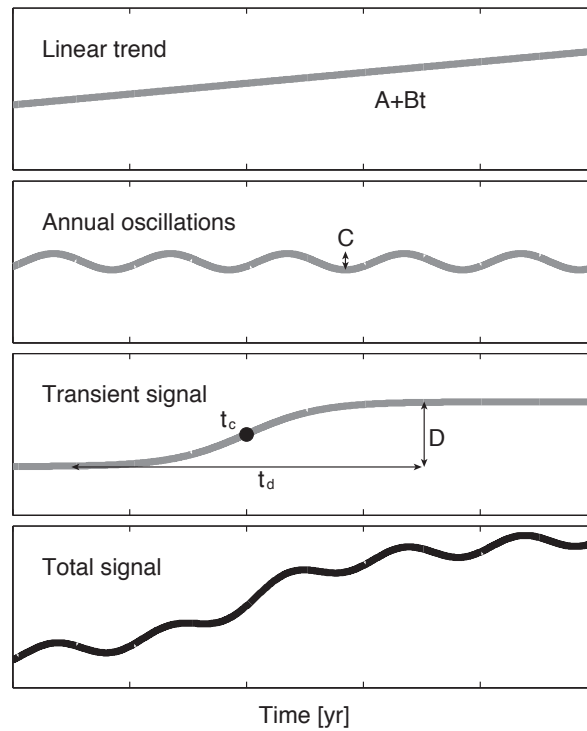


Figure 2. The CGPS time-series are modeled as a combination of a linear trend, annual oscillations and a transient uplift signal at Theistareykir with amplitude D , central time t_c and transient time t_d .

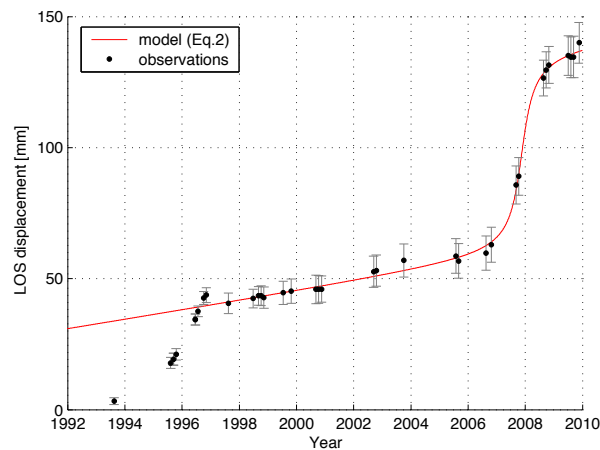


Figure 3. Temporal evolution of line-of-sight (LOS) displacement at Theistareykir central volcano, derived from InSAR time-series-analysis. The results show two periods of uplift, one before 1997 and another between 2007 and 2009, as well as steady-state plate-boundary motion. The temporal deformation evolution after 1997 was modeled according to Equation (2).

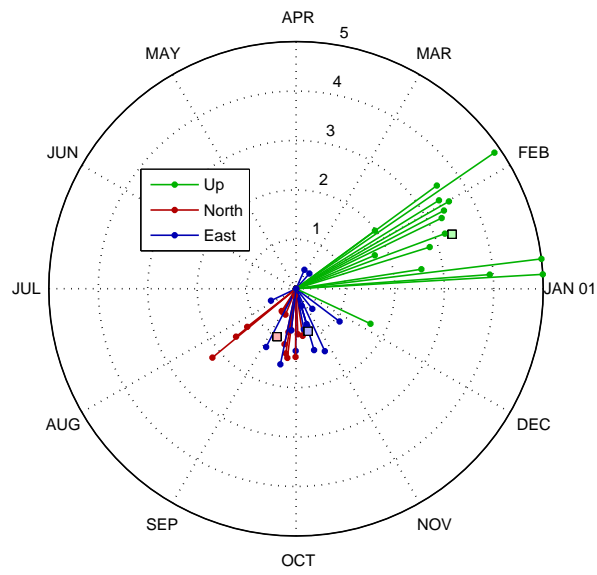


Figure 4. Phasor plot of estimated annual oscillation peaks and amplitudes (in mm) in the CGPS time-series. The squares mark the weighted mean of the peak shift and amplitude for each component.

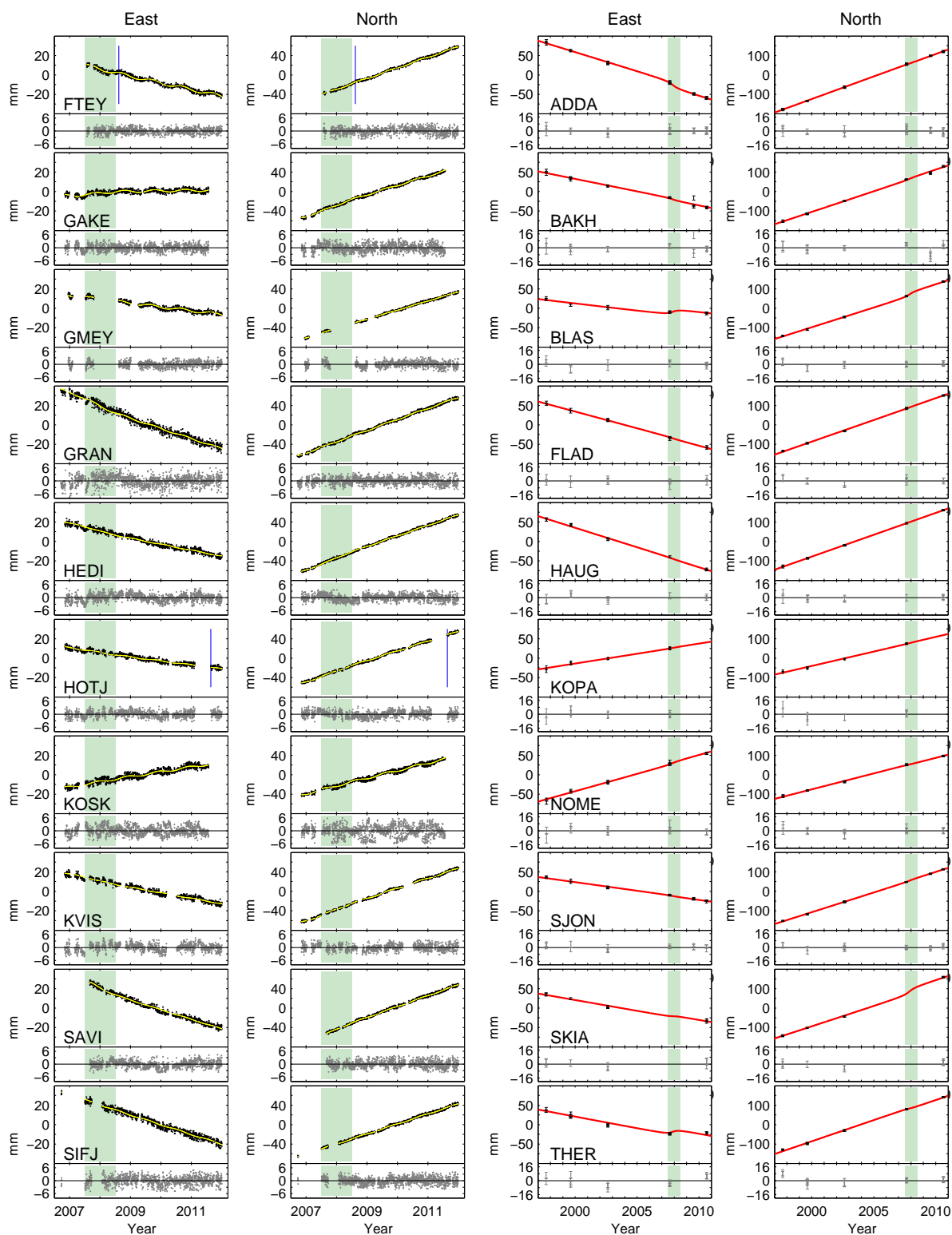


Figure 5. A selection of continuous (left) and campaign (right) horizontal GPS time series (black dots, for station location refer to Fig. 1). The model prediction (yellow/red) accounts for steady inter seismic deformation, the volcanic uplift transient at Theistareykir in 2007-2009 (shaded in green) and seasonal oscillation (for CGPS data). Residuals are shown in the lower part of each subfigure (gray dots). The CPGS data are corrected for antenna changes (indicated by blue lines).

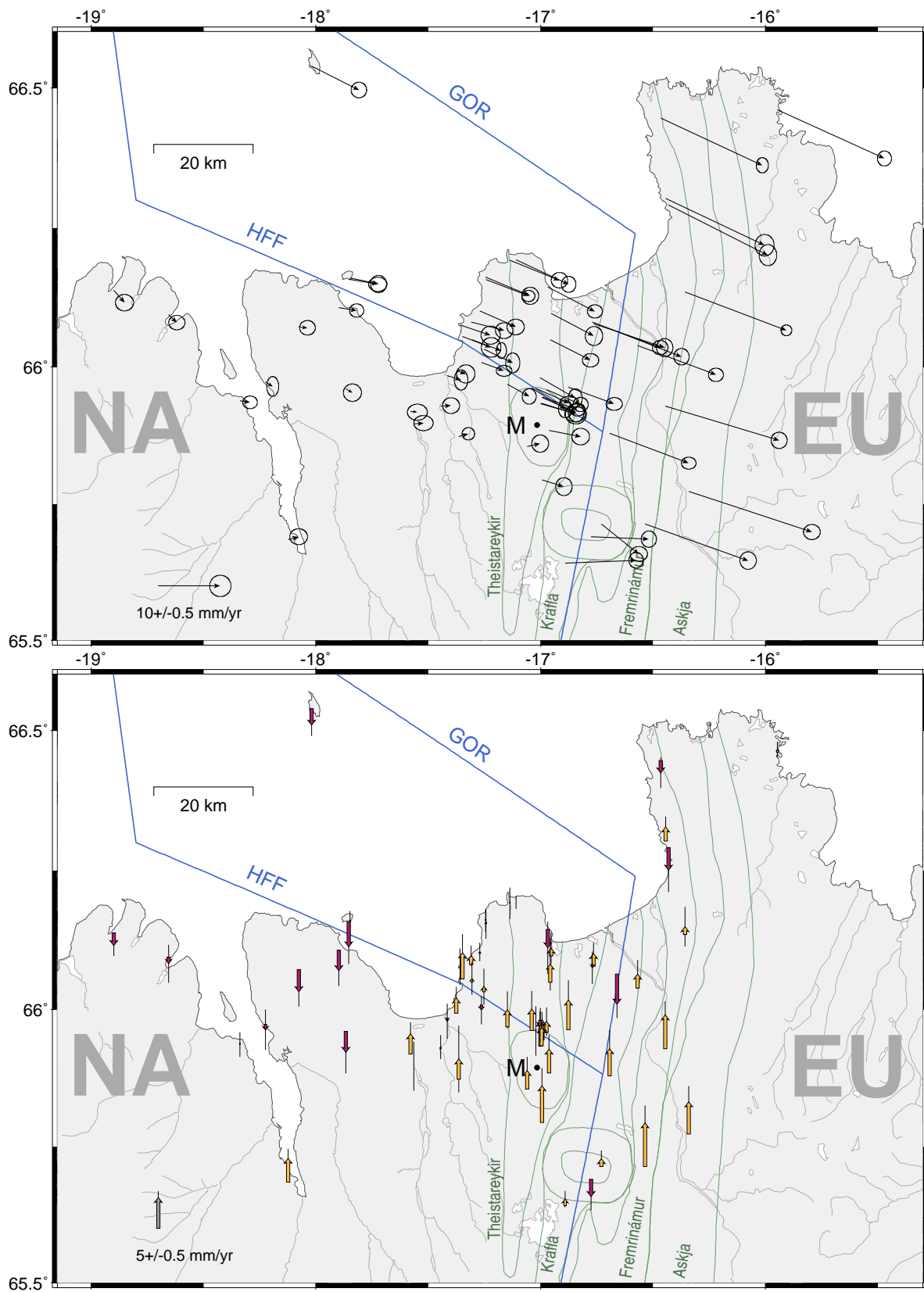


Figure 6. Horizontal (top) and vertical (bottom, purple: subsidence, yellow: uplift) GPS velocities with 95% (top) and 68% (bottom) confidence levels, after correcting for the Theistareykir uplift transient, simulated with the Mogi source M. Green lines outline fissure swarms and central volcanoes. The blue lines indicate the segments of the interseismic deformation model. The reference frame of the upper figure is based on fixed North America (MORVEL), but slightly modified with an offset vector of ~ 4 mm yr⁻¹ obtained from the modeling (Section 6).

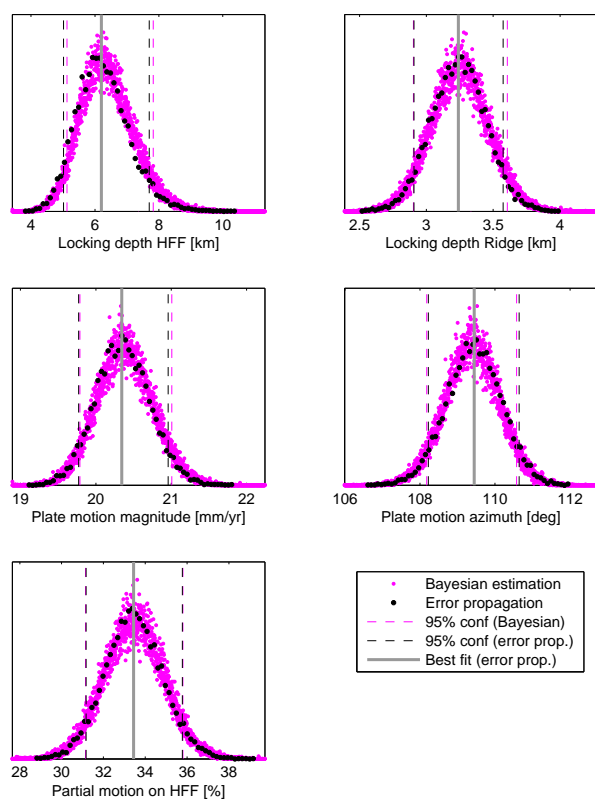


Figure 7. Estimations of the posterior marginal probability density functions for the TFZ model parameters using two different methods: Error propagation and Bayesian estimation.

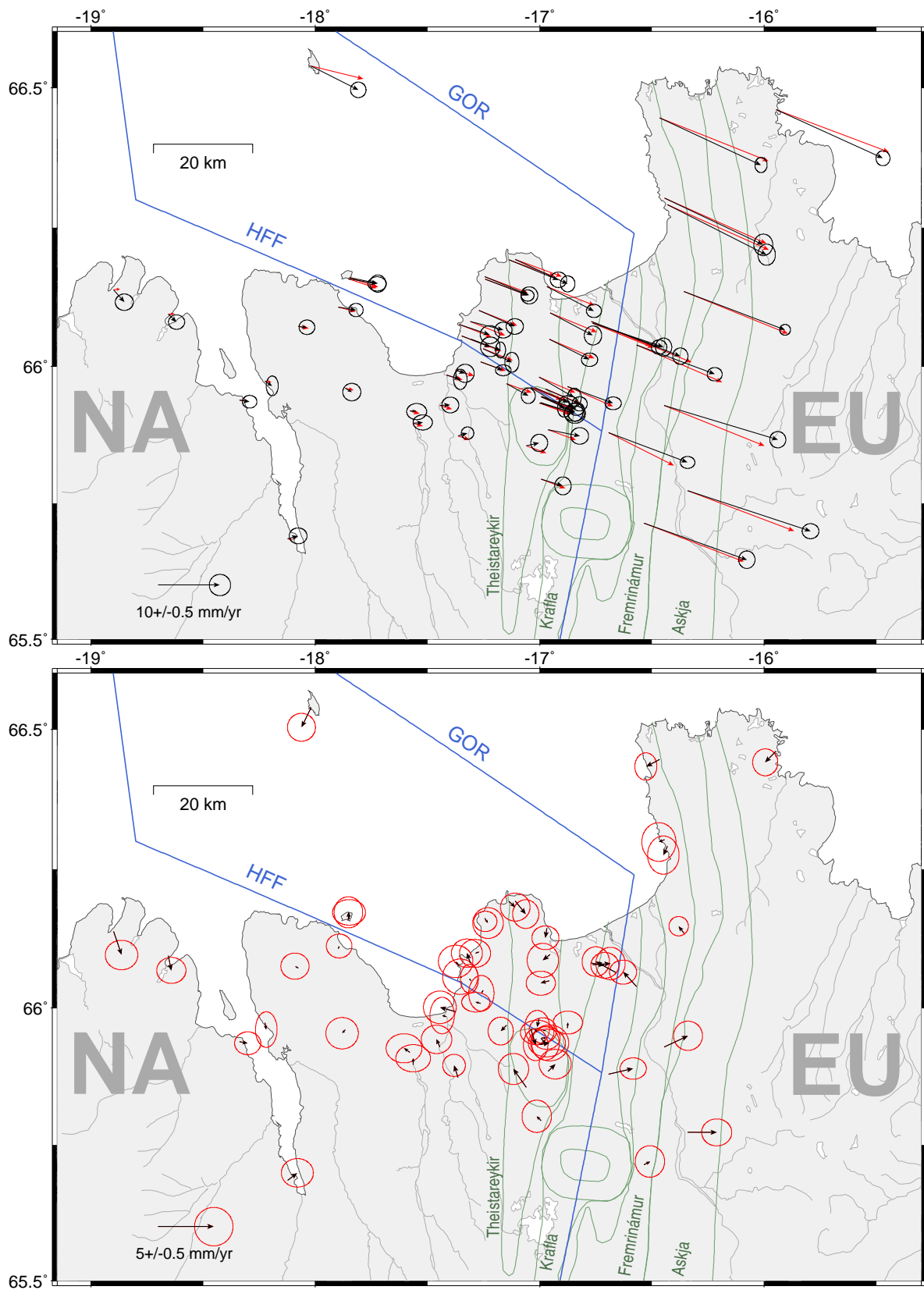


Figure 8. Velocity predictions (above) of the best-fit model (red) in comparison to the observations with 95% confidence level (black) and the residual signal between the two. Mind the different scale. The blue lines indicate the segments of the interseismic deformation model. The reference frame is based on a stable North America but modified with shift parameters obtained from the modeling (Chapter 6).